

An Investigation of Oxygen Availability in Spreading Fires

Alexandra N. Howell and Erica L. Belmont (10)*, Department of Mechanical Engineering, The University of Wyoming, 1000 E. University Ave, Laramie, WY, USA

Sara S. McAllister and Mark A. Finney, Missoula Fire Sciences Laboratory, US Forest Service, 5775 US Highway 10 W, Missoula, MT, USA

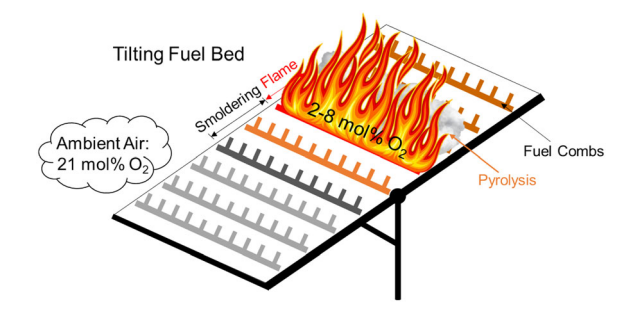
Received: 7 November 2022/Accepted: 1 March 2023

Abstract. Wildfire spread models that couple physical transport and chemical kinetics sometimes simplify or neglect gas-phase pyrolysis product oxidation chemistry. However, empirical evidence suggests that oxygen (O₂) is available for gas-phase and solid-phase combustion within the flaming reaction zone. This study addresses outstanding questions of O₂ availability by directly measuring O₂ concentrations near fuel surfaces within spreading fuel bed fires for the first time. Temporally and spatially resolved O₂ concentrations within laboratory fires were investigated using uniform fuel beds of medium density fiberboard (MDF) and cardboard (CB) combs at various packing ratios (β) and angles. Minimum O₂ concentration reached approximately 2-5 mol\% for most fuel beds of higher β (> 0.010), while some fuel beds of low β (≤ 0.010) exhibited higher minimum O₂ concentrations up to 8 mol%. Flame rate of spread, residence time, and minimum O_2 were found to vary with β and were influenced by bed angle within a given β . Thermogravimetric analysis was used to assess O2 availability impacts on flaming and smoldering fuel consumption rates. Negligible impacts were observed for initially unburned fuels at ambient O2 concentrations of $\leq 10 \text{ mol}\%$, but O_2 availability had significant impacts on char oxidation rates at all tested concentrations. A one-dimensional diffusion model of O2 availability at char surfaces for near-particle O2 concentrations tested and measured in TGA and fuel bed experiments revealed a strong dependence of O2 availability on mass flux from the particle. The results of this work provide new insights regarding O₂ availability and inert assumptions for fire spread models.

Published online: 01 June 2023

^{*}Correspondence should be addressed to: ; Erica L. Belmont, E-mail: ebelmont@uwyo.edu

Graphical Abstract



Keywords: Wildfire, Oxygen (O2) availability, Fire spread, Char oxidation, Thermogravimetric analysis

1. Introduction

Wildland fire is a naturally occurring global phenomena that has been studied for many decades, but which is still not fully understood [1-4]. Knowledge of the physical and chemical fundamentals of fire behavior is necessary to predict rates and directions of spread to support operational decision making and firefighter safety, understand impacts of wildland fire on ecological environments for effective forest management and rehabilitation, and assess the influences of fire dynamics on atmospheric processes and global climate [1, 3, 5–9]. This is a challenging objective for the spatially and temporally variable, chaotic process that is wildfire and which is further complicated by the heterogeneous weather, landscapes, and fuels in which wildfires occur [1, 3, 10–13]. Due to this complexity and variability, fire behavior and rate of spread (RoS) models must make significant simplifications and assumptions about fire kinetics and transport phenomena, and no currently available predictive models can provide all the necessary information for all relevant situations. Some assumptions utilized in current models have been developed without experimental basis, but are now being re-examined as increased computational power facilitates new model capabilities and improved experimental methods and instrumentation enables sampling in previously inaccessible fire environments [5, 8, 13, 14].

Current RoS models range from simple rules-of-thumb to computationally expensive simulations. The simpler models are generally used to assist forest and fire managers in making real-time decisions during fire events, while the more complex computational models are not practical for aiding in operational decision making but are being developed to help advance knowledge of the fundamental processes that drive fire dynamics [2, 5, 9, 13, 15–18]. Of the six model categories identified by Sullivan [5], only physical models consider the coupled fundamental behavior of physical transport and chemical kinetics to predict fire directionality, RoS, and combustion products. The aim of these physical models is to capture coupled physics and chemistry such that critical fire behavior can be simulated

and therefore predicted for a given set of initial and boundary conditions [5, 8, 13, 17]. Experimental validation of approximations in available physical models is often limited [1–3, 5, 8, 14, 19–21].

The complexity of modelling wildland fuel combustion dynamics originates partly from highly temperature sensitive chemistry during the thermal degradation and oxidation of biomass fuels and partly because of the immense variation in fuel configurations (e.g., particle sizes and packing density) [13, 22-24]. Oxidation of the gas-phase volatiles produced during pyrolysis leads to flaming combustion, which occurs in a thin flame region where the hot gases from pyrolysis mix with available ambient oxygen (O₂). Flaming combustion has been identified as the primary source of heat generation needed for sustained flame spread [3]. Heterogeneous solid-phase char oxidation also occurs, often observed in the smoldering region behind the leading flame zone and which significantly impacts quantities of generated combustion products, including carbon dioxide (CO₂) emissions and solid char deposits [1, 25–31]. Sullivan [1, 3] and others [6–8, 69, 70] have identified that the reaction rates of homogeneous gasphase and heterogeneous solid-phase combustion differ by orders of magnitude. Thus, while flaming and smoldering oxidation reactions can occur simultaneously within the flaming reaction zone, much of the char oxidation occurs after the rapidly progressing flame front has passed. Empirical data suggest that differences in O₂ availability contribute to different burning behaviors, such as in open and densely packed fuel beds [24, 32–34]. Furthermore, the characterization of post-fire products has suggested that the limited O₂ present within the flaming zone significantly influences the physicochemical properties of fire-generated chars [7, 35–38].

Biomass thermal degradation and combustion chemistry is often neglected in physical models or reduced to one- or two-step global reactions in the gas phase, and involving only one or two gas-phase species [39-55]. Consequently, there is presently a gap between advanced kinetics models developed for thermal fuel degradation and the implementation of these kinetics models into physical models [22, 23, 56-59]. Accurate knowledge of the O₂ availability in wildland fuel beds during fire spread could improve physical models significantly, as most mechanisms currently employ inert assumptions despite the oxidative ambient conditions in which wildfires occur [3, 20, 34, 60]. These inert assumptions are based on advection of product gases away from fuel surfaces and consumption of available O₂ during oxidation of gaseous pyrolysis products, leading to limited O₂ availability at fuel surfaces [3, 24, 34, 35, 61]. Only two physical fire spread models currently consider any oxidation kinetics: FIRETEC, a coupled multiphase transport wildland fire model developed by Los Alamos National Laboratory (USA), and IUSTI, a multiphase reactive and radiative model using a heterogeneous combustible medium developed by Institut Universitaire des Systèmes Thermiges Industriels (France). Even so, FIRETEC and IUSTI only investigate oxidation in the gas phase using simple global reaction pathways and a few chemical species [5]. Solid-phase oxidation of the char is not considered even though coarse fuels can contribute significantly to total fuel consumption through this mechanism.

To date, there has been little experimental quantification of O_2 concentrations in fuel bed fires, or assessment of the role of O_2 availability on burning rates of wildland fuels within the flaming and smoldering reaction zones during fire

spread. There has been extensive research into the influence of variable ambient O₂ concentrations on pyrolysis and gas-phase oxidation of biomass during heating and burning [10, 56, 58, 59, 62–65], but few direct measurements of O₂ concentrations at fuel surfaces during fire spread have been reported. Korobeinichev et al. [14] used a microprobe coupled to a mass spectrometer to measure O₂ concentration profiles in downward flame spread along a single vertical pine needle and observed minimum O₂ concentrations of approximately 2 to 5 mol% when the microprobe was positioned 1 to 2 mm from the pine needle. The microprobe mass spectrometry method was further utilized by Joshi et al. [66] to measure the O₂ concentration distribution in downward flame spread through multiple parallel fuel sheets, where similar minimum O2 concentrations within the flame were observed, and results were used to develop a flame spread model in OpenFOAM. Shotorban et al. [67] used an oxidative pyrolysis model, FDS-Gpyro3D, to simulate the O₂ concentration at the surface of a single isolated burning leaf and showed minimum concentrations of 0-5 mol\%. The FDS-Gpyro3D model utilized in [67] was developed using experimental data reported by Pickett et al. [68]. However, Pickett et al. [68] did not directly measure O₂ concentrations at leaf surfaces and, thus, the O₂ concentrations at the fuel surface simulated in [67] have not been experimentally validated. These limited results indicate that O2 is not completely depleted at fuel surfaces during flaming combustion, as is often assumed.

The present study addresses unexplored questions of O₂ availability inside fuel beds in spreading fires and assesses the impacts of O₂ on flaming and smoldering burning behavior and resulting fuel consumption. Time-resolved O₂ concentrations within spreading fires were directly measured for fuel beds composed of medium density fiberboard (MDF) and cardboard (CB) combs, using uniformly packed fuel beds at various packing ratios and slope angles. The measured O₂ concentration profiles were transformed into a reference frame of position relative to the O₂ probe location within the bed in order to identify extent and duration of O₂ depletion within three reaction zones: the pyrolysis region ahead of the flame, the flame zone, and the smolder region behind the flame. Further investigation was performed using thermogravimetric analysis (TGA) to assess the impacts of O₂ availability on flaming and smoldering oxidation rates of MDF and CB fuels at ambient O₂ concentrations measured in the spreading fires of this study. Lastly, a one-dimensional (1D) mass transport model was used to estimate O₂ concentrations at char fuel surfaces based on near-particle O2 availability. The results of this work provide novel data and insights regarding fuel consumption during spreading fires and the appropriateness of O2 availability assumptions used in physical fire spread models.

2. Materials and Methods

2.1. Experimental Apparatus and Fuels

Measurement of O₂ concentrations within fuel beds was performed in spreading fires using the Missoula Fire Sciences Laboratory (MFSL) tilting fuel bed appara-

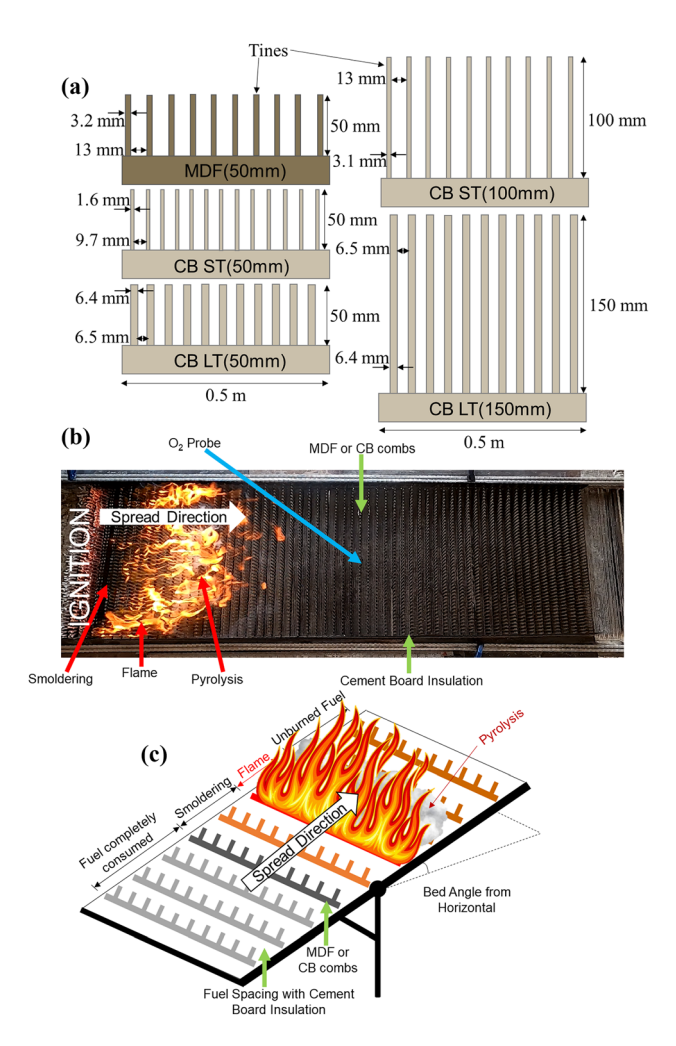


Figure 1. (a) Medium density fiberboard (MDF) and cardboard (CB) comb types investigated in this study. The CB combs included small tine (ST) and large tine (LT) varieties. Tines are indicated at the top of (a). The MDF comb tine depth was 2.9 mm and all CB comb tine depths were 1.4 mm. The tine widths, heights, and gap spacing of each comb type are identified. The fuel combs were packed into the Missoula Fire Sciences Laboratory (MFSL) tilting fuel bed apparatus, shown in (b) viewed from the top and (c) illustrated from an oblique perspective, and combs were separated by cement board insulation spacers. Pyrolysis, flaming, and smoldering regions are indicated. The location of the $\rm O_2$ probe within the fuel bed is identified, and ignition is initiated from the left side of the bed as situated in (b), such that fire spread was from left to right. The bed angle from horizontal is indicated in (c).

tus with bed dimensions of approximately 0.5 m and 1.6 m in width and length, respectively. Medium density fiberboard (MDF) and cardboard (CB) fuels of different sizes were investigated over a range of bed packing ratios (β), defined as the fraction of bed volume filled with fuel, and angles from horizontal. The MDF and CB had densities of 720 and 600 kg/m³, respectively. The fuels were laser cut using a commercial CO₂ laser system to resemble vertically oriented fuel particles in a wildland environment, with a solid spine supporting multiple individual tines, similar in shape to large combs (Fig. 1a). The fuel combs were packed into the MFSL tilting fuel bed by inserting the spine of the comb into the bed such that only the tines were exposed above the bed surface [20, 71].

Five fuel comb types of different sizes were utilized in this study and are illustrated in Fig. 1a. All investigated tine sizes can be classified as 1-h fuels [24]. One MDF comb type was investigated and had tine dimensions of 50, 2.9, and 3.2 mm for the height, depth, and width of each tine, respectively, and with a gap width of 13 mm between each tine. This MDF comb type is hereafter referred to as MDF (50 mm). Four CB comb types with different tine sizes and gap spacing were investigated, and these are coarsely categorized as two small tine (ST) CB comb types and two large tine (LT) CB comb types. The two CB ST comb types had tine heights of 50 and 100 mm, referred to as CB ST (50 mm) and CB ST (100 mm), respectively, and the two CB LT comb types had tine heights of 50 and 150 mm, referred to as CB LT (50 mm) and CB LT (150 mm), respectively. Tine widths and gap spacing for each of the four CB comb types can be viewed in Fig. 1a. All CB comb types had the same tine depth of 1.4 mm.

Fuel bed packing was done by inserting MDF and CB combs at predetermined positions along the axial length of the bed, and between 6.4 mm-wide spacers of insulating cement board material. The location of the O_2 probe within the fuel bed and important flame features are identified in Fig. 1b and discussed in further detail in Sects. 2.2 and 2.3, respectively. Eight fuel bed densities were investigated where combs were spaced with 18, 16, 14, 10, 8, 6, 4, or 2 cement board spacers between each fuel comb such that combs were positioned every 114, 102, 88.9, 63.5, 50.8, 38.1, 25.4, or 12.7 mm along the axial length of the bed, respectively. The bed packing ratio (β) is determined for the specific packing of each fuel bed test using Eq. 1, which is equivalent to the bulk density of the bed over the fuel particle density,

$$\beta = \frac{V_p}{V_{p+g}} = \frac{w_p * h_p * t_p}{\left(w_p + w_g\right) * h_p * \left(t_p + t_g\right)} \tag{1}$$

and where V_p is the volume of a single comb tine particle and V_{p+g} is the volume of a single tine particle and the gap volume between that tine and the next. The calculation of these volumes is also shown in Eq. 1 in terms of the particle and gap widths perpendicular to the direction of spread, w_p and w_g respectively, the particle and gap depth in the direction of spread, t_p and t_g respectively, and the height of the fuel particle, h_p , which is identical to the height of the gap.

Once the bed was packed with fuel combs at the predetermined β , the bed was tilted and locked into place at 20, 25, 30, 35, or 40° from the horizontal. The naming convention of each fuel comb type, packing, and angle is as follows: Height)"_"Number Type" "Tine Type(Tine of Insulating ers"i "Angle". For example, a bed packed with CB LT(50 mm) combs, packed between 8 insulating spacers each, and angled to 30° is indicated CB LT(50 mm) 8i 30°. The test matrix of all fuels, packing, and bed angles investigated in this work is provided in Supplementary Information using the described nomenclature. Not all combinations of packing density, bed angle, and fuel comb type were tested due to a lack of flame spread under some parameter combinations, where a lack of flame spread was identified as the inability of the flame to propagate the entire length of the bed. Once a set of bed parameters was identified as unable to spread reliably, it was eliminated from further investigation and not included in this study. The bed packing combinations that failed to spread were primarily those with the lowest packing ratios ($\beta \le 0.010$) at shallow angles (< 25°). Increasing the bed angle was needed for such low packing ratio fuel beds to overcome the significant gaps between fuel layers that inhibited flame spread. All MDF and CB fuels were conditioned in the ambient environment such that they had a moisture content (MC) of approximately 3-8 wt% prior to burning in all testing scenarios except one set of tests using CB LT(50 mm) conditioned to 15-20 wt% MC, denoted as WET_CB_LT(50 mm)_4i_40°.

Additional unique fuel bed configurations were explored to broaden the values of β investigated and evaluate the generality of the results using homogenous fuel beds. First, CB LT(50 mm) combs were stacked in duplicate and triplicate, referred to as CB_LT(50 mm)_4i_30°_dup and CB_LT(50 mm)_4i_30°_trip, respectively. The CB_LT(50 mm)_4i_30°_dup and CB_LT(50 mm)_4i_30°_trip combs were placed between cement board spacers and aligned within each packing location such that the comb tines were stacked in the direction of fire spread, simulating CB LT(50 mm) combs with tines of larger depths. Additionally, one triplicate-stacked case, denoted as CB_LT(50 mm)_4i_30°_trip_sheet, was explored where the comb tines were offset to occlude lateral spaces such that the stacked tines resembled a solid sheet of CB LT(50 mm) fuel as viewed in the direction of spread. Illustrations of front and side views of the CB LT(50 mm) stacked in triplicate, and in both aligned and sheet configurations, are provided in Supplementary Information (Fig. S1).

Second, three unique test cases of mixed fuel beds at a bed angle of 25° were investigated by alternating MDF(50 mm) and CB ST(50 mm) combs in the following ways, and with two insulation spacers between each comb: (1) one CB ST(50 mm) comb between each instance of MDF, referred to as AltMDF&1CB_ST(50 mm)_2i_25°, (2) two CB ST(50 mm) combs between each instance of MDF, referred to as AltMDF&2CB_ST(50 mm)_2i_25°, and (3) three CB ST(50 mm) combs between each instance of MDF, referred to as AltMDF&3CB_ST(50 mm)_2i_25°. The AltMDF&2CB_ST(50 mm)_2i configuration is illustrated in Supplementary Information (Fig. S1) as a visual example of these mixed bed configurations. In total, 34 bed configurations of fuel type, packing, and angle were tested (Table 1). Each test configuration was repeated at least

Table 1. Categories of packing ratio (β) investigated, with test configurations in each category identified by fuel type, fuel bed packing, and fuel bed angle. Similar values of β are grouped by number and labeled β 1 to β 8, and these categories are also identified by color throughout this study. Configurations marked with asterisks were tested once due to fuel availability or equipment limitations, while other configurations were tested at least twice.

	Packing Ratio (β) Range	Number of Tests in Category	Category Color	Configurations in Category	
β1	0.004-0.005	5	Blue	CB_ST(100mm)_8i_30°	CB_ST(50mm)_8i_35°
				CB_ST(50mm)_6i _35°	CB_ST(50mm)_8i_40°
				CB_ST(50mm)_6i_40°	
β2	0.006-0.010	9	Purple	CB_ST(50mm)_4i_25°	*CB_LT(150mm)_16i_30°
				CB_LT(150mm)_14i_30°	CB_ST(100mm)_6i_30°
				CB_ST(50mm)_4i_30°	*CB_LT(150mm)_18i_35°
				*MDF(50mm)_8i_35°	CB_ST(50mm)_4i_35°
				CB_ST(50mm)_4i_40°	
β3	0.011-0.015	5	Brown	*CB_ST(50mm)_2i_20°	*CB_LT(150mm)_10i_30°
				*MDF(50mm)_6i_30°	CB_ST(50mm)_2i_30°
				CB_LT(50mm)_8i_35°	
β4	0.016-0.020	3	Red	MDF(50mm)_4i_25°	CB_LT(50mm)_6i_30°
	0.010-0.020			*AltMDF&3CB_ST(50mm)_2i_25°	
β5	0.021-0.025	7	Orange	CB_LT(50mm)_4i_20°	*CB_LT(50mm)_4i_25°
				CB_LT(50mm)_4i_30°	CB_LT(50mm)_4i_40°
				WET_CB_LT(50mm)_4i_40°	
				*AltMDF&1C	B_ST(50mm)_2i_25°
				*AltMDF&2CB_ST(50mm)_2i_25°	
β6	0.036	2	Pink	*MDF(50mm)_2i_20°	MDF(50mm)_2i_30°
β7	0.048	5	Green	CB_LT(50mm)_2i_20°	CB_LT(50mm)_2i_25°
				CB_LT(50mm)_2i_30°	CB_LT(50mm)_2i_40°
				CB_LT(50mm)_4i_30°_dup	
β8	0.070	2	Black	CB_LT(50mm)_4i_30°_trip	*CB_LT(50mm)_4i_30°_trip_sheet

twice for statistical analysis, except for some unique bed or high fuel load cases that were tested once due to fuel availability limitations or to avoid damage to the O_2 analyzers.

Initial results suggested that the flaming and smoldering characteristics, and thus the extent and duration of O_2 depletion, depended highly on β , which has been previously theorized to influence airflow to the burning zone during fire spread [72, 73]. Several categories of similar β were identified and grouped, as outlined in Table 1, and values of investigated β ranged from 0.004 to 0.070. Fuel beds with β less than 0.04 were not included in this study due to lack of flame spread along the entire bed length observed during preliminary tests, where this flame spread failure was attributed to large spaces between fuel comb rows at such low β . Fuel beds with β greater than 0.070 were not tested in order to protect the O_2 analyzers, as large quantities of organic volatiles were emitted during burning of higher β beds that could damage sensitive instrument components. In total, eight β categories were identified and numbered as β 1 to β 8 from the lowest to the highest β values. All 34 fuel and bed configurations explored in this study are listed in Table 1 within their associated β category. These numbered β category

gories are used throughout the remainder of this study to assess impacts of β on burning characteristics and O_2 depletion extent and duration.

2.2. O₂ Measurement

Time-resolved O₂ concentrations were measured during each experimental burn using either an SPX Corporation Genisys Evo Scan Tool with a Gas M-P add-on module or an Enerac Model 700 Integrated Emissions System Analyzer. Good agreement within the average uncertainty of all O₂ measurements was found between the two instruments in tests with the same fuels and bed configurations. A stainless steel O₂ probe was inserted into the bottom of the tilting fuel bed and between cement board spacers such that the opening of the probe was flush with the tilting bed surface at the base of the fuel tines. The O₂ probe port was located approximately one-half to two-thirds of the fuel bed length upslope of the ignition location to permit the fire to reach a steady spread rate well ahead of the probe (Fig. 1b). Both gas analyzers had a sampling rate of 1 Hz and an instrument delay in response to changes in gas concentrations of approximately 2 s.

2.3. Characterization of Flame Properties

A GoPro camera was mounted above the tilting fuel bed for video recording of each test at 59.9 fps, and Fig. 1b shows a single video frame of a CB LT(50 mm) 4i 30° burn test. Fuel beds were ignited at the lower end of the tilted bed using approximately 25 g of excelsior and 6 mL of methanol, and the flame front was then allowed to self-propagate along the length of the fuel bed under ambient laboratory conditions. During each burn test, several distinct flame characteristics became apparent. After ignition and flame development, the flame zone progressed across the bed preceded by smoke and evolution of gaseous pyrolyzates. The arrival of this region to fresh fuel was noted to typically initiate a decrease in O₂ from the ambient level. Behind the flame zone, fuel tines typically continued smoldering until complete burnout, as indicated by the tines visibly reducing to ash and collapsing. The O2 levels remained reduced from the arrival of the pyrolysis zone to the time of complete burnout. Every tested fuel bed configuration exhibited these behaviors, with the thicknesses of pyrolysis, flaming, and smoldering regions, as well as the extent and duration of O₂ depletion, varying depending on fuel type, β , and slope angle.

The acquired videos were processed using Matlab to obtain flame and smolder rates of spread (RoS) and zone thicknesses for each fuel bed test using 40 frames isolated from each video, which were selected to capture flame front positions of approximately every 2 cm along the packed length of the fuel bed. The frames were cropped in the bed width direction to isolate 7–12 cm across the center of the bed, and approximately 160 cm of the center of the bed in the length direction, and converted to grayscale to determine a relative brightness within each frame, which was then used to determine the boundaries and propagation rates of the flame and smolder regions. The relative brightness was determined by summing the grayscale value of every pixel (values of 0–255, where 0 is black and 255 is white) at every bed location and taking the ratio of the actual summed value to

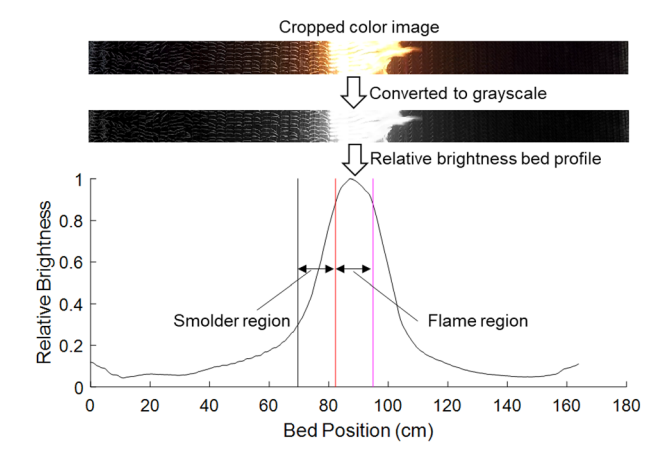


Figure 2. Example cropped image of a video frame in full color and grayscale (top and middle, respectively) acquired during a fuel bed test burn. Flame and smolder region boundaries were determined using relative brightness. The flame region was estimated using bounds of 85-95% of the maximum relative brightness, and the smolder rear boundary was determined as 25-35% of the maximum relative brightness. The flame boundaries are illustrated using pink (flame front) and red (flame rear) vertical lines and the smolder boundaries are represented by red (smolder front) and black (smolder rear) vertical lines.

that if all the pixels were white. If all the pixels in the actual image were white, the relative brightness would have a value of 1. An example of this relative brightness analysis is shown in Fig. 2 using a single frame. The rear locations of the identified flame and smolder regions were used to determine the RoS of those features as they propagated across the bed. Generally, the flame boundaries were found to be accurately captured by using a boundary threshold of approximately 85–95% of the maximum relative brightness. Similarly, the rear smolder boundary was found to be accurately captured using a boundary threshold of approximately 25-35% of the maximum relative brightness. These boundary thresholds were critically analyzed for each video of each burn and adjusted as needed to accurately capture the flame and smolder thicknesses observed for each video. Values for flame and smolder RoS and thicknesses were determined as an average of the results derived from the 40 frames that were assessed. The statistical uncertainties determined for the flame and smolder RoS and thicknesses were low using 40 frames, with values less than approximately 5% of the average values. Thus, uncertainties in the flame and smolder RoS and thicknesses were assessed as variations in replicate fuel bed test values using standard deviation.

The flame and smolder RoS were used to reframe time-resolved O_2 concentration measurements in terms of position in the fuel bed relative to the O_2 probe location. The time at which the rear of the flame was located directly over the O_2 probe was identified from the videos and used to calculate the relative position of

each time-resolved O_2 concentration value from that initial position. This was done by using the flame and smolder RoS and each time step before and after the initial position to calculate the value of each relative position, resulting in O_2 concentration profiles across the fuel bed at a single time during the test. Additional details about this relative position calculation can be found in Supplementary Information (Fig. S2). These O_2 profiles with respect to relative position were then used to study the flame and smolder regions, as well as identify the pyrolysis regions within the O_2 profiles by overlaying the locations of the flame and smolder boundaries estimated from the video analysis onto the O_2 concentration profiles with respect to position. The pyrolysis region was determined as the difference between the location where the O_2 concentration initially decreased below 20 mol% and the leading edge of the flame.

2.4. Burning Rates

Additional investigation of O₂ availability effects on MDF and CB flaming and smoldering oxidation rates was performed at the fuel particle scale using a TA Instruments Discovery 5500 Thermogravimetric Analyzer (TGA). Samples were heated at 500°C/min to simulate rapid heating, ignition, and oxidation in the MFSL tilting fuel bed as closely as possible, MDF(50 mm), CB ST(50 mm) and CB LT(50 mm) comb tines were cut into approximately 6 mm-long pieces to fit into 100 µL platinum TGA pans, resulting in sample masses of approximately 34, 12 and 17 mg, respectively. Mass and temperature calibrations were performed for each gas environment, and the following environments were tested based upon O₂ concentrations measured in the tilting fuel bed tests: (1) inert, 100 vol% N₂, (2) 98/2 vol/vol% N₂/O₂, (3) 95/5 vol/vol% N₂/O₂, (4) 92/8 vol/vol% N₂/O₂, (5) 90/ 10 vol/vol% N_2/O_2 , (6) 85/15 vol/vol% N_2/O_2 , and (7) simulated air, 80/20 vol/ vol% N₂/O₂. All N₂/O₂ gas environment combinations had a total flow rate of 100 mL/min. A minimum of two replicates was performed for each of the three fuel particle types and in each gas environment, and standard deviation was used to assess uncertainty.

Two sets of TGA tests were performed in each gas environment. First, unburned comb tine samples were heated at 500°C/min to 700°C to investigate impacts of O₂ availability on oxidation rates. The upper temperature limit of 700°C was selected because all tine types underwent complete devolatilization by approximately 600°C. Second, char oxidation rates were isolated to determine impacts of O₂ availability on this slower phase of combustion by subjecting charred tines to the oxidative gas environments. Unburned fuel was charred by heating the particles to 700°C at 500°C/min in 100 vol% N₂ to fully pyrolyze the particles, and then the charred particles were cooled in N₂. Subsequently, the remaining char residue was oxidized by heating at 500°C/min to 950°C in one of the aforementioned oxidative environments.

2.5. O₂ Diffusion Model

A one-dimensional (1D) mass transport model was developed to estimate O₂ availability at the surface of a CB LT(50 mm) particle in the oxidative gas envi-

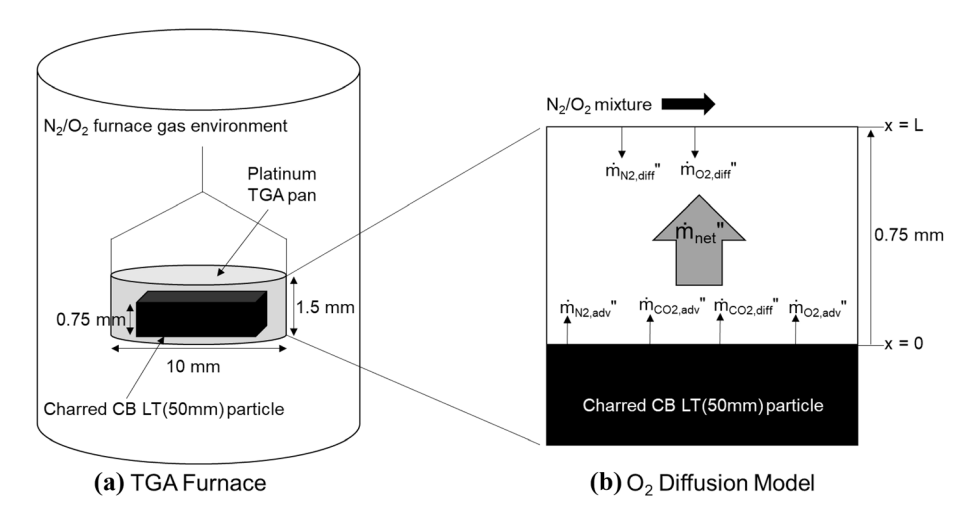


Figure 3. (a) Schematic of TGA furnace and sample pan in which charred CB LT(50 mm) particles were subjected to N_2/O_2 gas mixture environments. (b) Schematic showing components considered in one-dimensional (1D) mass transport model of char oxidation.

ronments that were explored using the TGA. Schematics of the TGA furnace and O_2 diffusion model are provided in Fig. 3.

The general 1D expression for species A diffusion through a binary mixture on a mass basis is

$$\dot{m}_{A}^{"} = Y_{A} \left(\dot{m}^{"} \right) - \rho D_{AB} \frac{dY_{A}}{dx}. \tag{2}$$

where $\dot{m}_{A}^{"}$ is the net mass flux of species A, Y_{A} is the mass fraction of species A, \dot{m} is the total net flux of the gas mixture per unit area, ρ is the bulk density of the species A and B mixture, and D_{AB} is the binary diffusion coefficient for diffusion of species A into species B [74, 75]. Three primary gas species were considered in the O2 diffusion model: N2 and O2 which flow across the top of the open sample pan, and CO₂ which was assumed to be the primary combustion product species. The net gas mixture mass flux from the pan (\dot{m}) was derived from TGA char mass loss data collected during the char oxidation experiments described in Sect. 2.4. The charred particle was assumed to be pure carbon, and the mass loss data was used to calculate net CO2 and O2 mass fluxes from and to the charred particle. The distance over which O2 must diffuse from the surroundings to the charred CB particle surface was assumed to be 0.75 mm which is half the depth of the TGA platinum pan. Boundary conditions are known for N₂, O₂, and CO₂ in the far-field (x = 0.75 mm) based on environment gas composition. Binary diffusion coefficients for each species were determined using the ideal gas equation of state, the mean molecular speed, and the mean free path relationship at each TGA temperature during oxidation experiments, which results in a calculation of the coefficient based on the mass of the gas species, and system temperature and pressure [74]. The bulk density was approximated as that of air at each temperature during the oxidation experiments.

Three equations were solved to determine the three species concentration distributions— Y_{N2} , Y_{CO2} , and Y_{O2} —in the modelled system (Fig. 3b). Equation 2 was simplified for N_2 by setting the net flux (\dot{m}_{N2}) to zero because N_2 is an inert gas in the system and is not produced or consumed. Using a far-field boundary condition of $Y_{N2}(x=L) = Y_{N2,L}$ where $Y_{N2,L}$ is known based on the imposed TGA gas environment, Eq. 2 was solved to yield an expression for the mass concentration of N_2 within the TGA sample pan

$$Y_{N2}(x) = Y_{N2,L} \exp\left(\frac{\dot{m}''}{\rho D_{N2-m}}(x-L)\right)$$
 (3)

where D_{N2-m} is the diffusion coefficient for the diffusion of species N_2 into the mixture of species CO_2 and O_2 [76].

The concentration profile of CO_2 (Y_{CO2}) was determined using Eq. 2 and a boundary condition of $Y_{CO2}(x=L)=0$, and the mass concentration distribution of CO_2 throughout the modelled 1D system is

$$Y_{CO2}(x) = \frac{\dot{m}_{CO2}^{"}}{\dot{m}^{"}} \left(\frac{\exp\left(\frac{-\dot{m}^{"}x}{\rho D_{CO2-m}}\right)}{\exp\left(\frac{-\dot{m}^{"}L}{\rho D_{CO2-m}}\right)} - 1 \right). \tag{4}$$

The net flux of CO_2 (\dot{m}_{CO2}^*) was determined from TGA mass loss data and the ratio of the molecular weight of CO_2 to that of pure carbon.

Similarly, for O_2 , there is a mass flux of O_2 within the system due to the consumption of O_2 in oxidative reactions at the particle surface. Using Eq. 2 and a boundary condition of $Y_{O2}(x=L)=Y_{O2,L}$, where $Y_{O2,L}$ is known from the imposed ambient gas environment, the concentration distribution of O_2 is

$$Y_{O2}(x) = \frac{\dot{m}_{O2}''}{\dot{m}''} + \frac{\exp\left(\frac{-\dot{m}''L}{\rho D_{O2-m}}\right) \left(Y_{O2,L} - \frac{\dot{m}_{O2}''}{\dot{m}''}\right)}{\exp\left(\frac{-\dot{m}''x}{\rho D_{O2-m}}\right)}.$$
 (5)

The net flux of O_2 ($\dot{m}_{O2}^{"}$) was determined from TGA data, where the char carbon mass loss was used to determine the net flux of O_2 based on an assumption of carbon oxidation to CO_2 . The mixture diffusion coefficients, D_{N2-m} , D_{CO2-m} , and D_{O2-m} , were determined using the general form

$$D_{N2-m} = \frac{1 - Y_{N2} \left(\frac{m}{MW_{N2}}\right)}{\frac{Y_{CO2} \left(\frac{m}{MW_{CO2}}\right)}{D_{N2-CO2}} + \frac{Y_{O2} \left(\frac{m}{MW_{O2}}\right)}{D_{N2-O2}}}$$
(6)

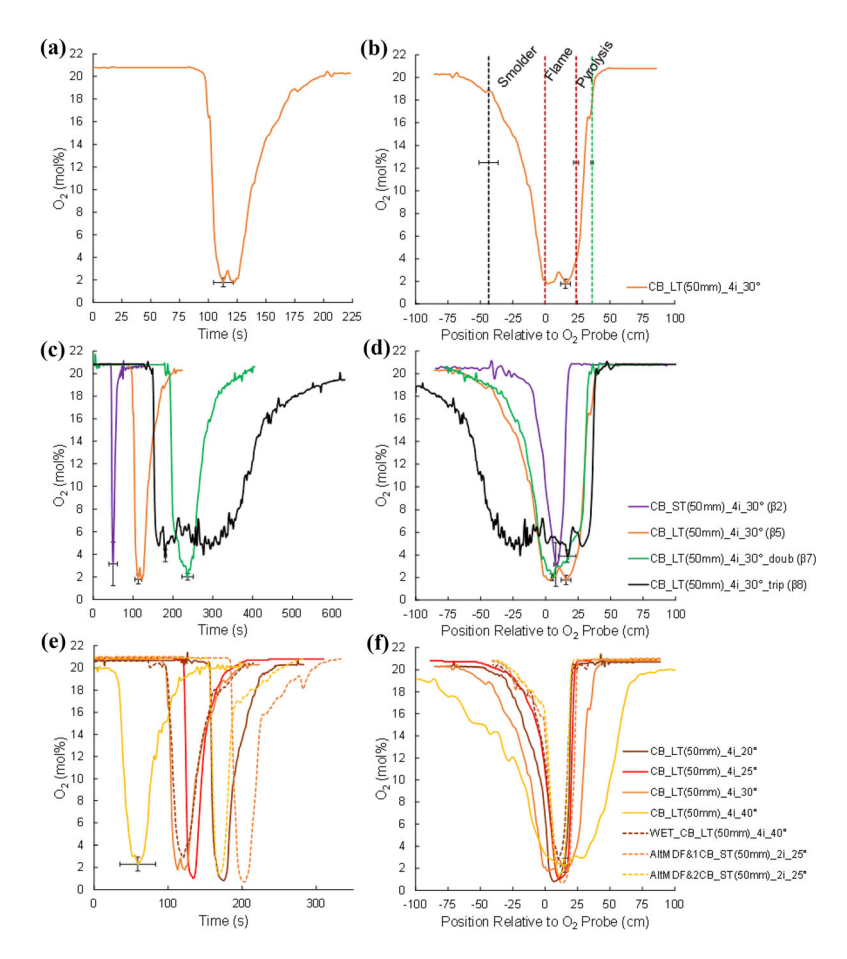


Figure 4. O_2 concentration profiles with (a) time and (b) position relative to the O₂ probe for CB_LT(50 mm)_4i_30°. Pyrolysis, flame and smolder regions are indicated in (b) with the uncertainty of the boundary locations for each region shown. The impacts of packing ratio (β) on extent and duration of O_2 depletion are compared in terms of (c) time and (d) position for a range of β categories including β 2 (smallest shown), β 5, β 7, and β 8 (largest). Fuel bed tests in the β 5 category are compared with respect to (e) time and (f) position. Uncertainty for the minimum O₂ concentration, time, and position for each O_2 profile is shown in (a-d), where O_2 concentration and time uncertainties are due to experimental variability and position uncertainty derives from propagation of uncertainty applied to the transformation of O_2 concentration in time to position. The average uncertainty of the minimum O_2 concentration, time, and position for all repeated configurations in the β 5 category (Table 1) is shown in (e) and (f).

where m is the total mass of the overall gas mixture of species N_2 , CO_2 and O_2 .

The resulting model has 6 unknowns (Y_{N2} , Y_{CO2} , Y_{O2} , D_{N2-m} , D_{CO2-m} , and D_{O2-m}) and six equations (Eqs. 3, 4, 5, and Eq. 6 for D_{N2-m} , D_{CO2-m} , and D_{O2-m}) and was solved using a numerical solver to determine the concentration of O_2 at the charred particle surface. This analysis was applied to simulate oxidation of charred CB LT(50 mm) at every temperature step during heating from approximately 200 to 900°C in order to investigate the impacts of near-particle O_2 availability on O_2 availability at particle surfaces and oxidation rates.

3. Results and Discussion

3.1. Oxygen Depletion Extent and Duration

Measured O_2 concentrations with respect to time and relative to the O_2 probe location are shown in Fig. 4 for CB_LT(50 mm)_4i_30°. Figure 4a and b show a single set of data in both frameworks. Pyrolysis, flame, and smolder regions are indicated in Fig. 4b, where the rear of the flame is located at the O_2 probe location and the other region boundaries are identified relative to that location. Though the entire bed length is shown in Fig. 4b, d and f, these relative positions were calculated using the steady-state flame and smolder RoS determined using data from the center 160 cm length of the bed to avoid any potential end effects. These reaction zone thicknesses are tabulated in Supplemental Information for all tested fuel bed conditions. A range of β in both frameworks is shown in Fig. 4c and d to highlight the impacts of β on O_2 depletion and duration. The flame region for the lowest β shown in Fig. 4c and d (β 2) is the narrowest, with a smolder region trailing the flame that is similar in size. As β increases, the flame thickness increases and the smolder region trailing the flame grows increasingly larger than the flame region due to the slower rate of solid-phase char oxidation.

Additionally, O_2 concentrations with respect to time and relative to O_2 probe location for all tested fuel beds in a single β category (β 5) are compared in Fig. 4e and f, and O_2 profile comparisons for all other β categories are provided in Supplementary Information. The profiles in Fig. 4e and f are presented in an orange color palette for consistency with the color selected to identify the β 5 category throughout this study. In Fig. 4e, O_2 depletion is offset based on different flame RoS, which is primarily affected by bed angle in beds of the same β and is attributed to increased convective heating further ahead of the flame zone in beds with increased angle. For example, a comparison of the O_2 profiles for CB_LT(50 mm)_4i at a variety of angles from 20 to 40° reveals that O_2 depletion begins earlier in time for the steepest angle and correspondingly fastest RoS. In addition to bed angle, other fuel bed effects on RoS can also be observed in Fig. 4e; notably, the mixed beds angled at 25° had the lowest spread rates among tested β 5 configurations, lower than even the shallowest tested angle in that category (CB LT(50 mm) 4i 20°).

Analysis of O₂ depletion behavior with respect to time is useful for assessing differences in flame propagation behavior, but comparisons of flame structure can

be more difficult to interpret in a time-based reference frame. The comparison of all tests in the β 5 category with respect to O_2 probe position (Fig. 4f) reveals a general similarity in flame characteristics in this β category with one exception. Notably, the O₂ depletion profile for CB LT(50 mm) 4i 40° exhibits a large reaction zone outside the statistical variability of all tests performed in category $\beta 5$, and this is attributed to the enhanced flame contact angle with unburned fuel at the steep 40° bed angle. Nonetheless, despite significant differences in fuel bed characteristics which included unique packing conditions AltMDF&2CB ST(50 mm) 2i 25° AltMDF&1CB ST(50 mm) 2i 25°, and WET CB LT(50 mm) 4i 40°, an analysis of O₂ concentration with position reveals that β can be used to group the burning behavior of fuel beds of different fuel types, sizes, packings, and angles. The impacts of β on flame and smolder RoS and thickness, O₂ depletion extent and duration, and the availability of O₂ for fuel oxidation are further explored in the remaining sections.

The minimum O_2 concentration for each tested fuel bed shown in Fig. 4 reached approximately 2–5 mol%, similar to that observed in [14] and [66]. A few fuel bed conditions not shown in Fig. 4, but discussed in ensuing sections, exhibited higher minimum O_2 concentrations up to 8 mol%. Additionally, O_2 concentrations in the smolder region were depleted, typically to < 15 mol%, for extended periods after the flaming zone had passed.

3.2. Impacts of Bed Packing Ratio (B)

Flame residence time, flame RoS, smolder RoS, and minimum O_2 are shown in Fig. 5a–d, respectively, for tested β and bed angles. The β categories (β 1 through β 8) are indicated by color, and error bars represent the average uncertainty for each β category. Fuel bed angle was varied within each β category and impacted flame residence time and RoS, smolder RoS, and minimum O_2 within a given β category. Bed angle effects are particularly noticeable within β 5 and β 7, where results suggest that flame residence time and rates of spread generally increased with bed angle, and minimum O_2 generally varied inversely with bed angle. However, additional testing would be required to evaluate the correlation strength of these flame characteristics with bed angle.

Flame residence time was found to increase linearly overall with β as expected [24, 72] and the linear trend is illustrated in Fig. 5a. Flame, smolder, and pyrolysis zone thicknesses were measured and found to not correlate strongly with β . These values are listed in Supplementary Information for reference and were used to calculate additional burning characteristics, including fuel surface area burning rate.

Flame and smolder RoS decreased rapidly with increases in β from 0.004 to approximately 0.020, after which the rate of change decreased significantly at higher β . The flame and smolder RoS exhibited similar behavior with respect to β , but the smolder RoS values were smaller in magnitude due to the slower rate of char oxidation [1, 3, 6–8, 69, 70]. The flame RoS values were similar to those reported by He et al. [72] and Catchpole et al. [77], but with larger RoS values at the lower β values tested in this study due to the variation of angle that significantly expanded the range of measurable β values by enabling fire to spread in

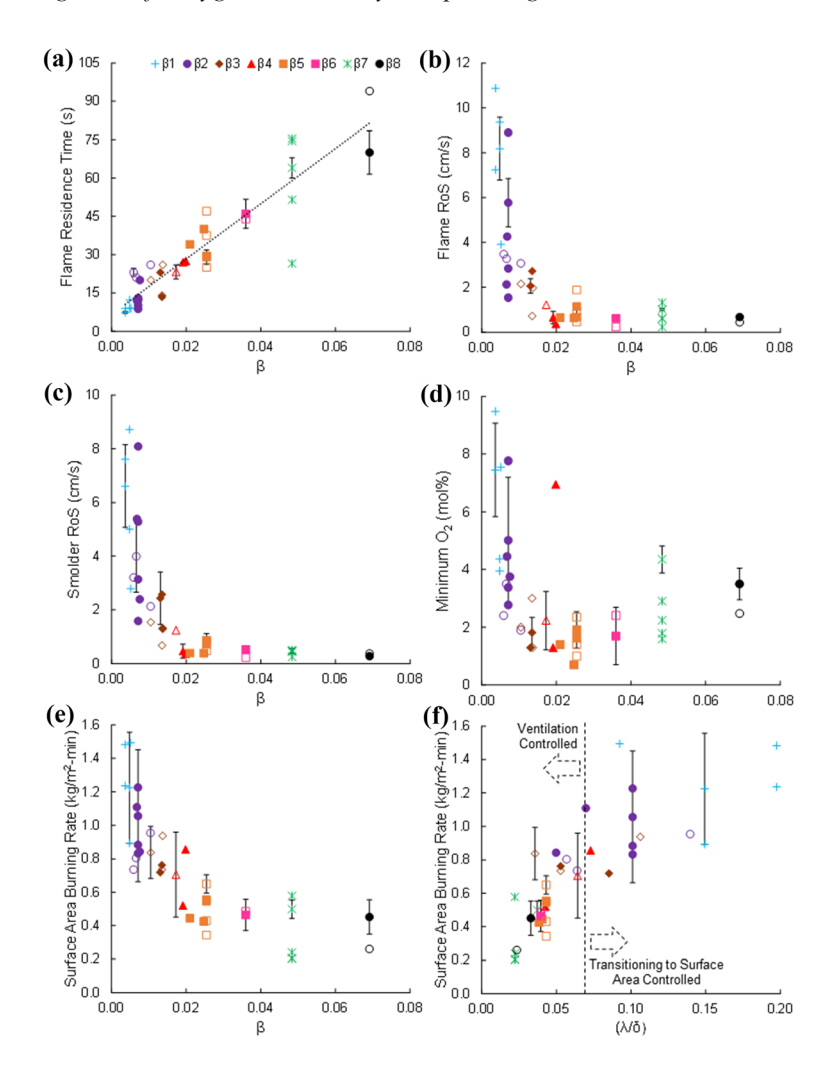


Figure 5. (a) Flame residence time, (b) flame rate of spread (RoS), (c) smolder RoS, and (d) minimum O_2 concentration with respect to packing ratio (β). The R^2 value of the linear trendline shown in (a) is 0.84. Categories of β are grouped and indicated by color. The surface area burning rate with respect to (e) β and (f) the dimensionless bed porosity factor (λ/δ) are also shown. For β 2- β 6 and β 8, filled markers indicate configurations which were repeated and open markers indicate configurations which were tested once (Table 1). The average uncertainty of repeated configurations in each β category is included for each plotted parameter (Color figure online).

very low β (< 0.010) beds at steep angles (\geq 30°). He et al. [72] postulated that the increase in void space between fuels at lower β allows more O_2 to enter the burning zone which promotes increased RoS due to the resulting enhanced temperature and heat transfer. Similarly, Finney et al. [24] noted that smaller void space between fuel particles limits the entry of air into the burning zone as fuel beds become denser at higher β , forcing the pyrolysis gases to oxidize farther above the fuel bed where more O_2 is available for combustion. The reduction of O_2 and gasphase oxidation rates within the flame zone decreases the temperature and radiative heat transfer of the burning zone, thus slowing the RoS. These theories are explored through O_2 measurements in this study and results of other studies [14, 66], where an increase in RoS has been observed to occur when greater O_2 concentrations were measured in fuel beds of low β .

The minimum O_2 concentration with respect to β exhibited similar behavior to flame and smolder RoS trends, though there were several outliers where the minimum O_2 of some fuel bed tests were significantly higher than others in the same β category. The outliers occurred in fuel bed tests that exhibited distinct behavior during experiments. First, increased variability in flaming and smoldering characteristics and O_2 depletion was observed with decreasing β , which was attributed to higher variability of fire spread versus extinguishment that depended upon nonsteady flame contact and convective heating across increasingly large fuel gaps. Fuel beds with very low β (< 0.010), such as β 1 and β 2, had to be adjusted to higher bed angles (≥ 25°) for fire spread to be successful due to the large gaps between fuel particles. Flame spread at low β was observed to be sensitive to the intermittency of flame contact needed for the ignition of unburned fuels and sustained flame spread. The fuel beds observed to be closest to extinguishment at very low β and having the highest minimum O_2 values shown in Fig. 5d were CB ST(50 mm) 4i 25° and MDF(50 mm) 4i 25. These two tests had relatively small flame thicknesses - 11 and 9.7 cm, respectively - and propagated at velocities of 1.54 and 0.37 cm/sec (Supplementary Information) and essentially one layer of fuel at a time, depleting the O₂ concentration from ambient for only a few seconds and resulting in higher minimum O2 values of 7.8 and 7.0 mol%, respectively.

The second observed behavior that induced higher minimum O₂ concentrations was strong circulation associated with towers and troughs parallel to the fire spread direction [20, 78–82]. This circulation behavior was particularly observed in this study for conditions which produced large flame thicknesses and/or high flame RoS. The tests that exhibited the strongest circulation behavior included CB_ST(100 mm)_8i_30°, CB_ST(50 mm)_8i_35°, and CB_ST(50 mm)_8i_40°, which resulted in RoS of 3.90, 7.24 and 10.9 cm/sec, respectively, and these tests also showed O₂ depletion for only a few seconds, with minimum values of 7.55, 7.63 and 7.45 mol%, respectively. The higher minimum O₂ concentrations may be attributable to the advective effects of the circulation behavior transporting more air into the fuel beds.

Notably, as the discussion above highlights, some beds that had large flame thicknesses also had fast RoS that resulted in short O₂ depletion times. Flame thickness is a difficult parameter to isolate because it is dependent on a variety of

bed factors, including bed angle and β , and no correlation was found between flame thickness and minimum O_2 (not shown). Flame RoS correlated weakly with minimum O_2 concentrations (Supplementary Information, Fig. S5). Results suggest that minimum O_2 concentration increased with an increase in RoS, although a linear trendline fitted to the data produced an R^2 of only 0.23.

Figure 5b-d show significant changes in burning behavior between low and high β , suggesting a transition in burning regimes. Two burning regimes—ventilation controlled and surface area controlled—have been identified in previous studies based on bed porosity (λ), or the ratio of void volume to fuel particle surface area in the bed [33, 61, 83]. Nelson [61] defined λ as

$$\lambda = \frac{1 - \beta}{\sigma \beta} [cm] \tag{7}$$

where σ is the surface area to volume ratio of each individual tine of the MDF or CB combs. Nelson [61] also recommended using a dimensionless porosity factor (λ/δ) , where δ is the height of the fuel and equal to 50, 100 or 150 mm in this study, to identify the transition between burning regimes. This transition theoretically occurs at $(\lambda/\delta) = 1$, but that threshold has been shown to differ signficantly for different fuels and packing.

The burning regimes in this study were further assessed in terms of fuel surface area burning rate, R_s , defined by [61] as

$$R_s = \frac{A_r \left(\frac{W_a}{\tau}\right)}{A_p} \left[\frac{kg}{m^2 - \min} \right] \tag{8}$$

where A_r is the projected area of the flame zone as viewed from a perspective normal to the bed, W_a is the fuel load in mass per projected area of the flame zone, τ is the reaction zone residence time, and A_p is the total fuel particle surface area in the reaction zone [61]. The reaction zone was determined to include both the flame and pyrolysis regions in the present work, comparable to the reaction zone defined by [61]; notably, a reaction zone utilizing solely the flame region was also investigated and found to produce the same burning rate trends but with higher magnitudes. Fuel load was calculated using Eq. 9,

$$W_a = \frac{m_p}{(t_p + t_g)(w_p + w_g)} \left[\frac{kg}{m^2} \right]$$

$$\tag{9}$$

where m_p is the particle mass.

Surface area burning rates with respect to β and (λ/δ) are presented in Fig. 5e and f. The surface area burning rate decreased with increased β , showing a similar trend to that observed for the flame and smolder RoS, while surface area burning rate increased with (λ/δ) . Results suggest the existence of two different burning regimes: ventilation controlled beds corresponding to densely packed fuel beds in which the surface area burning rate increases linearly with increasing (λ/δ) , or

decreasing β , and surface area controlled beds corresponding to loosely packed fuel beds in which the surface area burning rate is independent of (λ/δ) , and therefore β . The results in Fig. 5e and f suggest that fuel bed burning behavior was transitioning to the surface area controlled regime at the lower β and higher (λ/δ) investigated in this study but, as was observed in [61], a clear delineation between ventilation and surface area controlled regimes was not observed at lower β and larger (λ/δ) . For fuel beds within the ventilation controlled regime at the larger β and lower (λ/δ) in this study, burning was limited by the ability of air to advect into the reaction zone due to dense fuel bed packing, and minimum measured O_2 in this regime was generally 1–3 mol%. In the lowest β and highest (λ/δ) categories, where a suggested transition to a surface area controlled regime occurred, O_2 supply was less limited within the reaction zone and minimum measured O_2 in this regime was generally > 3 mol%.

3.3. Burning Rates

The development of Eq. 8 by Nelson [61] is based on the assumption that charring takes place outside of the flaming region or phase of combustion, thus not taking char oxidation into account. However, char oxidation has been shown to participate competitively with gas-phase oxidation in the flame zone [1, 3, 6–8, 69, 70]. The impacts of O₂ availability on derivative thermogravimetric fuel consumption rates (DTG in %/min) are presented in Fig. 6 for unburned fuels which undergo pyrolysis, flaming, and char oxidation, as well as pre-pyrolyzed chars which only undergo char oxidation. Figure 6a-c show results for the raw fuel, resulting from the combined pyrolysis and smoldering present in raw fuel combustion, while Figs. (d-f) show results for the charred fuel, resulting from the smoldering behavior of char alone. The experimental DTG profiles shown in Fig. 6 have been smoothed using a 5-point moving average to reduce noise, and error bars reflect the magnitude of the raw data deviation from the smoothed data. The DTG profiles of unburned CB LT(50 mm) heated in 20/80 mol% O₂/N₂ (simulated air), 15/85 mol% O₂/N₂, 10/90 mol% O₂/N₂, 8/92 mol% O₂/N₂, 5/95 mol% O₂/N₂, 2/98 mol% O₂/N₂, and 100 mol% N₂ are shown in Fig. 6a. Results differ negligibly as N₂ is decreased from 100 mol% N₂ to 10/90 mol% O₂/N₂ environments, but peak mass loss increases in higher O2 concentration environments.

Similar tests were performed for CB ST(50 mm) and MDF(50 mm), and peak DTG and temperature at the peak DTG for all three fuels are compared in Fig. 6b and c. Again, results show relatively little change in peak DTG from 100 mol% N_2 to 10/90 mol% O_2/N_2 , while the 15/85 mol% O_2/N_2 and 20/80 mol% O_2/N_2 environments show significant changes in peak DTG. Temperature at peak mass loss did not change significantly across oxidative environments even with a corresponding change in the peak DTG. Additionally, different impacts of O_2 availability on CB LT(50 mm), CB ST(50 mm) and MDF(50 mm) burning rates can be observed that are attributable to the particle tine size and type. For example, the CB ST(50 mm) particle exhibits higher DTG at lower temperatures than the CB LT(50 mm) particle due to the larger width of CB LT(50 mm) tines, which translates to a decrease in the surface area relative to the

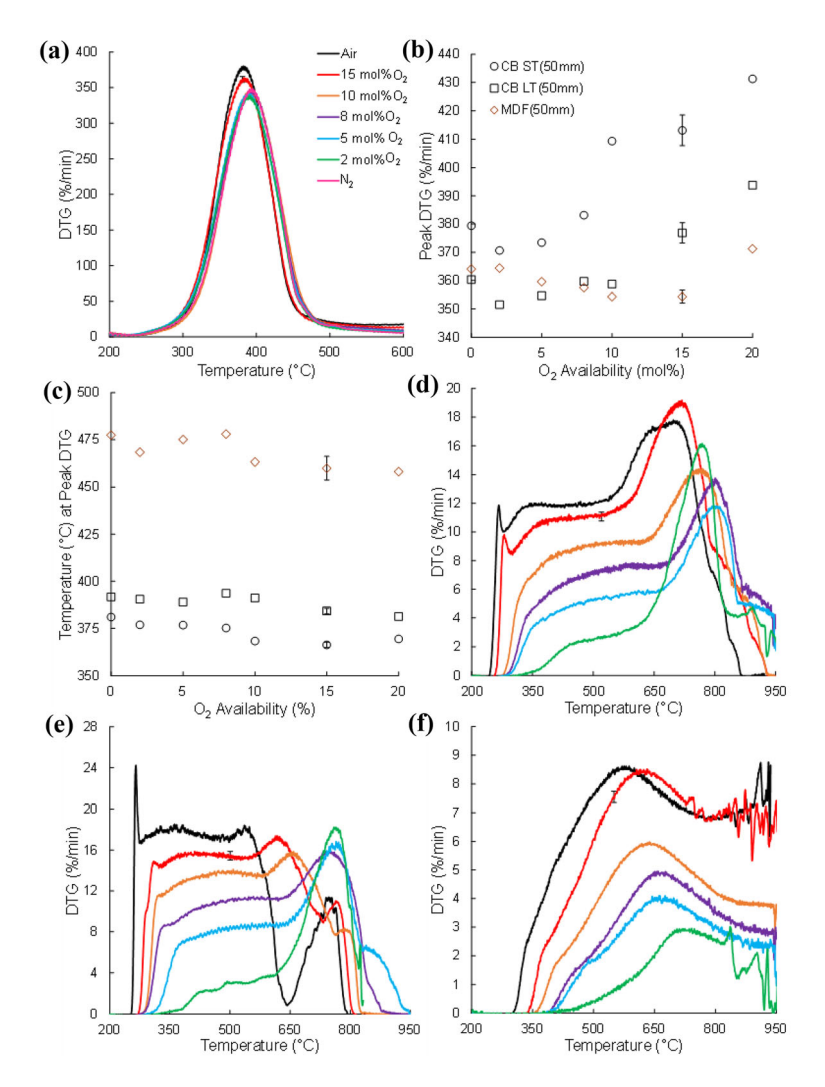


Figure 6. (a) Impacts of O_2 availability on derivative thermogravimetric (DTG) fuel consumption rates for CB LT(50 mm) as a function of temperature. (b) A comparison of peak DTG for CB LT(50 mm), CB ST(50 mm) and MDF(50 mm). (c) Temperature at peak DTG for CB LT(50 mm), CB ST(50 mm) and MDF(50 mm). Impacts of ambient O_2 levels on DTG fuel consumption rates are shown for pre-pyrolyzed (d) CB LT(50 mm) char, (e) CB ST(50 mm) char, and (f) MDF(50 mm) char. The legend in (a) also applies to (d-f), and the legend in (b) applies to (c). The uncertainty of the data presented in (a) and (d-f) was determined as the standard deviation of the data from the presented smoothed profiles and is representative of data noise. The error bars illustrated in (a) and (d-f) represent the average uncertainty determined for all DTG profiles shown. Uncertainty in (b) and (c) is an average of all results for each fuel category.

mass and increases transport limitations in the CB LT(50 mm) particle. The MDF(50 mm) shows reduced peak DTG (Fig. 6b) at significantly higher temperatures (Fig. 6c) as compared to the CB particles due to greater density and mass, which also increase transport limitations. Overall, the differences between inert and oxidative environments on peak DTG (Fig. 6b) and the temperature at peak DTG (Fig. 6c) for all investigated fuels were insignificant: all oxidative peak DTG and temperatures at peak DTG varied by less than 14 and 4%, respectively, from those measured for the N₂ environment. Excluding the three gas environments with the highest O₂ concentrations (air, 15 mol% O₂ and 10 mol% O₂), the changes in the peak DTG and temperature at peak DTG of the oxidative environments relative to the N₂ environment were less than 2.5 and 2%, respectively.

The negligible changes in peak DTG and temperature at peak DTG in gas environments of concentrations up to 10 mol% O₂ during pyrolysis and oxidative consumption of fuels (Fig. 6b and c) suggest that O₂ concentrations available for char oxidation are negligible under these conditions, supporting the inert assumptions utilized in many physical fire spread models [3, 20, 34, 60]. This range of O₂ concentrations up to 10 mol% differs slightly from the range of minimum O₂ concentrations measured in the spreading fuel comb fires that were designated as ventilation controlled in the present study (Fig. 5d and f). Differences in the thresholds of the ventilation controlled regimes for the fuel bed ($\sim 3 \text{ mol}\% \text{ O}_2$) and the TGA ($\sim 10 \text{ mol}\% \text{ O}_2$) are attributed to differences in the experimental platforms themselves. The TGA system is approximately 1D and available O2 can flow to the particle fuel surface from one direction only, limiting O₂ flux to the fuel surface and resulting in a ventilation limit at a higher ambient O₂ condition of 10 mol%. Still, the burning behavior observed in these TGA results is generally consistent with O₂ results in Fig. 5, where beds with the greatest void space (lowest β) that appear in transition to a surface area controlled burning regime were less O₂ limited. Taken together, these results suggest that pyrolysis was a significant controlling factor in fuel consumption rates for both the fuel bed and TGA and in both the surface area and ventilation controlled regimes. In the surface area controlled regime, significant quantities of O2 were available but burning rates were limited by pyrolysis rates. In the ventilation controlled regime, fuel consumption rates were limited by the advection of pyrolyzates away from fuel surfaces that prevented O₂ infiltration to the fuel bed.

To further investigate the effects of O₂ availability on char oxidation rates, prepyrolyzed CB LT(50 mm), CB ST(50 mm), and MDF(50 mm) char particles were oxidized in 20/80 mol% O₂/N₂ (air), 15/85 mol% O₂/N₂, 10/90 mol% O₂/N₂, 8/92 mol% O₂/N₂, 5/95 mol% O₂/N₂, and 2/98 mol% O₂/N₂, and DTG oxidation rates are presented in Fig. 6d–f, respectively. Char oxidation exhibited lower mass loss rates than unburned fuels (Fig. 6a and b) due to the slower rate of char oxidation as compared to devolatilization [1, 3, 6–8, 69, 70]. Additionally, peak DTG occurred at higher temperatures for char oxidation as compared to oxidation of unburned fuels. Results showed significant impacts of O₂ availability on char oxidation rates, which were observed to generally decrease with decreasing O₂ availability, although peak DTG values were generally higher at lower O₂ concentrations when ignition occurred at higher temperatures.

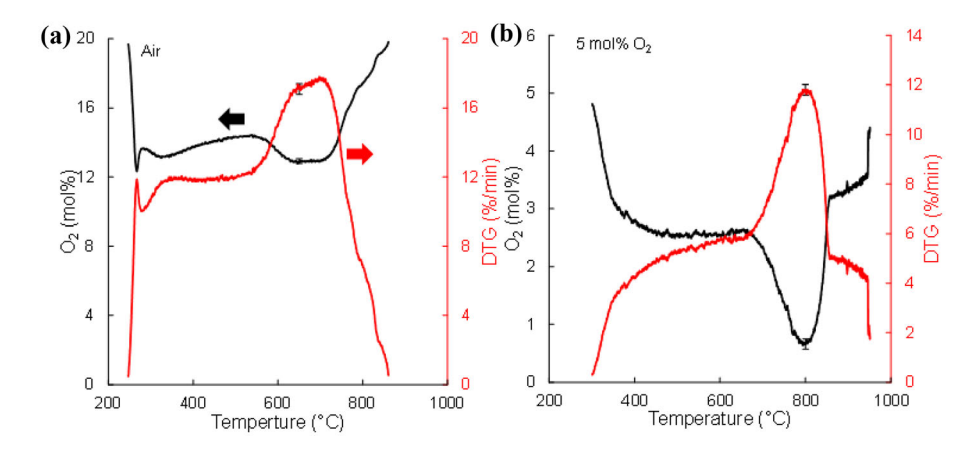


Figure 7. Results of the 1D mass diffusion model used to estimate O_2 concentrations at CB LT(50 mm) char particle surfaces in (a) 20/80 mol% O_2/N_2 and (b) 5/95 mol% O_2/N_2 TGA furnace gas environments. The O_2 concentrations at the particle surface are shown in black and the derivative thermogravimetric mass loss rate (DTG) profiles are shown in red. Uncertainty is the average deviation of the raw data from the smoothed profiles.

The impacts of ambient O2 availability on char oxidation rates can be better understood through an estimation of O2 concentrations at the char surfaces. Concentrations of O₂ present at CB LT(50 mm) char surfaces in TGA experiments, modeled using the 1D mass diffusion model outlined in Sect. 2.5, are presented in Fig. 7a and b for 20/80 and 5/95 mol\% O₂/N₂ furnace environments, respectively, over the range of DTG profiles that were measured from approximately 200 to 900°C (Fig. 6d). Again, DTG profiles were smoothed using a 5-point moving average. The results for 2, 8, 10, and 15 mol% O2 environments and for CB ST(50 mm) and MDF(50 mm) char particles are not presented for brevity but exhibited similar behavior to those of CB LT(50 mm) char in 20 and 5 mol\% O₂. For all environments, the O₂ concentration at the fuel surface was found to depend significantly on DTG magnitude. Under large mass fluxes indicated by large DTG, O2 availability was reduced at the particle surface as observed for both 20 and 5 mol\% O₂ environments in Fig. 7. Concentrations of O₂ at the char surface approached 0.5 mol% in 5 mol% ambient O2 and at high DTG (Fig. 7b). In contrast, O₂ depletion at the char surface in 20 mol% ambient O₂ was not significant (Fig. 7a), suggesting that O₂ availability is not negligible under some ambient conditions and should be considered in the development of future fire spread models.

4. Conclusions

Temporally and spatially resolved O₂ concentrations at the base of spreading fires were experimentally quantified for the first time, with the goal to inform physical fire spread models on the use of inert and oxidative assumptions. Medium density fiberboard (MDF) and cardboard (CB) fuel combs were burned over a range of packing ratios (β) and bed angles, and O₂ concentrations in the pyrolysis, flaming, and smoldering regions of the fire were measured. Results show that O₂ concentration was significantly depleted as the fire passed through the fuel bed, with minimum O₂ concentrations reaching approximately 2-5 mol% in almost all cases, and minimum O₂ concentrations as high as 8 mol% measured for beds with very low β . Flame characteristics, including flame and smolder rates of spread (RoS) and thicknesses as well as surface area burning rates, were assessed for the range of tested β and bed porosity (λ/δ) . Surface area burning rate variation with λ/δ suggested a gradual transition between ventilation and surface area controlled behavior over the range of tested conditions, and O₂ was found to be more suppressed in the ventilation controlled regime and less limited in the transition to a surface area controlled regime.

The impacts of O_2 availability on unburned fuel and char oxidation rates were further explored using thermogravimetric analysis (TGA). Availability of O_2 had negligible impacts on unburned fuel consumption rates at ambient O_2 concentrations of 10 mol% and below, but O_2 availability had significant impacts on char oxidation rates at all tested concentrations. Diffusion of O_2 to char fuel surfaces was assessed using a 1D model to estimate the amount of O_2 available to participate in solid-phase char oxidation based on near-particle O_2 availability. The O_2 concentration at char surfaces was found to depend strongly on the mass flux of combustion products from char particles during char oxidation, and model results suggest that O_2 availability at fuel surfaces may not be negligible as current fire models often assume. The results of this work provide new insights into the availability of O_2 within spreading fires and the impact of O_2 availability on fuel consumption rates for the improvement of current fire models.

Acknowledgements

This research was funded by NSF Award No. 2033379.

Author contributions

AH: conceptualization, design, methodology, experimentation, data analysis, writing. EB: conceptualization, funding acquisition, design, methodology, experimentation, data analysis, writing, supervision. SM: conceptualization, design, methodology, experimentation, manuscript review. MF: conceptualization, design, methodology, experimentation, manuscript review.

Declarations

Conflict of interest The authors declare that they have no known competing financial interests or personal relationships that could have appeared to influence the work reported in this paper.

SUPPLEMENTARY INFORMATION

The online version contains supplementary material available at https://doi.org/10.1007/s10694-023-01396-6.

References

- Sullivan AL (2017) Inside the inferno: fundamental processes of wildland fire behaviour: part 1: combustion chemistry and heat release. Curr For Rep 3:132–149. https://doi.org/10.1007/s40725-017-0057-0
- Yedinak KM, Strand EK, Hiers JK, Varner JM (2018) Embracing complexity to advance the science of wildland fire behavior. Fire 1:1–8. https://doi.org/10.3390/ fire1020020
- Sullivan AL (2017) Inside the inferno: fundamental processes of wildland fire behaviour: part 2: heat transfer and interactions. Curr For Rep 3:150–171. https://doi.org/10.1007/s40725-017-0058-z
- 4. Finney MA, Cohen JD, McAllister SS, Jolly WM (2012) On the need for a theory of fire spread. Int J Wildl Fire 107:25–36
- 5. Sullivan AL (2009) Wildland surface fire spread modelling, 1990–2007. 1: physical and quasi-physical models. Int J Wildl Fire 18:349. https://doi.org/10.1071/wf06143
- Surawski NC, Sullivan AL, Roxburgh SH, Meyer CPM, Polglase PJ (2016) Incorrect interpretation of carbon mass balance biases global vegetation fire emission estimates. Nat Commun 7:1–5. https://doi.org/10.1038/ncomms11536
- Santín C, Doerr SH, Merino A, Bucheli TD, Bryant R, Ascough P, Gao X, Masiello CA (2017) Carbon sequestration potential and physicochemical properties differ between wildfire charcoals and slow-pyrolysis biochars. Sci Rep 7:1–11. https://doi.org/10.1038/s41598-017-10455-2
- 8. Sullivan AL (2020) Physical modelling of wildland fires. Canberra, Australia
- 9. Greenlee JM (1982) Wildland fire modeling and strategy assessment. Fire Technol 18:237–250. https://doi.org/10.1007/BF02473136
- Viegas DXFC, Raposo JRN, Ribeiro CFM, Reis LCD, Abouali A, Viegas CXP (2021)
 On the non-monotonic behaviour of fire spread. Int J Wildl Fire 30:702–719. https://doi.org/10.1071/WF21016
- 11. Pérez Y, Pastor E, Àgueda A, Planas E (2011) Effect of wind and slope when scaling the forest fires rate of spread of laboratory experiments. Fire Technol 47:475–489. https://doi.org/10.1007/s10694-010-0168-7
- 12. Li H, Liu N, Xie X, Zhang L, Yuan X, He Q, Viegas DX (2021) Effect of fuel bed width on upslope fire spread: an experimental study. Fire Technol 57:1063–1076. https://doi.org/10.1007/s10694-020-01031-8
- 13. Morvan D (2011) Physical phenomena and length scales governing the behaviour of wildfires: a case for physical modelling. Fire Technol 47:437–460. https://doi.org/10.1007/s10694-010-0160-2

- Korobeinichev OP, Shmakov AG, Osipova KN, Kumar A, Meetei NK (2018) Experimental study and numerical modeling of downward flame spread along a sigle pine needle: part 1 (experiments). Combust Sci Technol 190:164–185. https://doi.org/10.1016/j.combustflame.2018.07.019
- 15. Jain P, Coogan SCP, Subramanian SG, Crowley M, Taylor S, Flannigan MD (2020) A review of machine learning applications in wildfire science and management. Environ Rev 28:478–505. https://doi.org/10.1139/er-2020-0019
- Cruz MG, Alexander ME (2019) Comments on "evaluating crown fire rate of spread predictions from physics-based models". Fire Technol 55:1919–1925. https://doi.org/ 10.1007/s10694-019-00856-2
- 17. Hoffman CM, Canfield J, Linn RR, Mell W, Sieg CH, Pimont F, Ziegler J (2016) Evaluating crown fire rate of spread predictions from physics-based models. Fire Technol 52:221–237. https://doi.org/10.1007/s10694-015-0500-3
- Josephson AJ, Castaño D, Koo E, Linn RR (2021) Zonal-based emission source term model for predicting particulate emission factors in wildfire simulations. Fire Technol 57:943–971. https://doi.org/10.1007/s10694-020-01024-7
- 19. Sullivan AL (2009) Wildland surface fire spread modelling, 1990–2007. 2: empirical and quasi-empirical models. Int J Wildl Fire 18:369. https://doi.org/10.1071/wf06142
- Finney MA, Cohen JD, Forthofer JM, McAllister SS, Gollner MJ, Gorham DJ, Saito K, Akafuah NK, Adam BA, English JD, Dickinson RE (2015) Role of buoyant flame dynamics in wildfire spread. Proc Natl Acad Sci USA 112:9833–9838. https://doi.org/10.1073/pnas.1504498112
- Finney MA, McAllister SS (2011) A review of fire interactions and mass fires. J Combust . https://doi.org/10.1155/2011/548328
- 22. Sullivan AL (2007) Competitive thermokinetics and non-linear bushfire behaviour. Dept Theor Physics, Res Sch Phys Sci Eng ANU Coll Sci PhD
- Sullivan AL, Ball R (2012) Thermal decomposition and combustion chemistry of cellulosic biomass. Atmos Environ 47:133–141. https://doi.org/10.1016/j.atmosenv.2011.11.022
- 24. Finney MA, McAllister SS, Grumstrup TP, Forthofer JM (2021) Wildland fire behaviour: dynamics, principles and processes. CSIRO Publishing, Melbourne
- 25. Santín C, Doerr SH, Preston CM, González-Rodríguez G (2015) Pyrogenic organic matter production from wildfires: a missing sink in the global carbon cycle. Glob Chang Biol 21:1621–1633. https://doi.org/10.1111/gcb.12800
- 26. Albini FA (1976) Estimating wildfire behavior and effects: General Technical Report INT-30. Intermountain Forest and Range Experiment Station
- López-Martín M, González-Vila FJ, Knicker H (2018) Distribution of black carbon and black nitrogen in physical soil fractions from soils seven years after an intense forest fire and their role as C sink. Sci Total Environ 637–638:1187–1196. https://doi.org/ 10.1016/j.scitotenv.2018.05.084
- Weise DR, Wright CS (2014) Wildland fire emissions, carbon and climate: characterizing wildland fuels. For Ecol Manage 317:26–40. https://doi.org/10.1016/j.foreco.2013.02.037
- 29. Jones MW, Santín C, Van Der WGR, Doerr SH (2019) Global fire emissions buffered by the production of of pyrogenic carbon. Nat Geosci 12:742–747. https://doi.org/10.1038/s41561-019-0403-x
- Bird MI, Wynn JG, Saiz G, Wurster CM, McBeath A (2015) The pyrogenic carbon cycle. Annu Rev Earth Planet Sci 43:273–298. https://doi.org/10.1146/annurev-earth-060614-105038

- 31. Huang X, Rein G (2017) Downward spread of smouldering peat fire: the role of moisture, density and oxygen supply. Int J Wildl Fire 26:907–918. https://doi.org/10.1071/WF16198
- 32. Kashiwagi T, Ohlemiller TJ, Werner K (1987) Effects of external radiant flux and ambient oxygen concentration on nonflaming gasification rates and evolved products of white pine. Combust Flame 69:331–345. https://doi.org/10.1016/0010-2180(87)90125-8
- 33. Gross D (1962) Experiments on the burning of cross piles of wood. J Res Natl Bur Stand—C Eng Instrum 66: 99–105
- 34. Boonmee N, Quintiere JG (2005) Glowing ignition of wood: the onset of surface combustion. Proc Combust Inst 30 II:2303–2310. https://doi.org/10.1016/j.proci.2004.07.022
- 35. Belcher CM, Hudspith VA (2016) The formation of charcoal reflectance and its potential use in post-fire assessments. Int J Wildl Fire 25:775–779. https://doi.org/10.1071/WF15185
- 36. Schneider MPW, Hilf M, Vogt UF, Schmidt MWI (2010) The benzene polycarboxylic acid (BPCA) pattern of wood pyrolyzed between 200°C and 1000°C. Org Geochem 41:1082–1088. https://doi.org/10.1016/j.orggeochem.2010.07.001
- 37. Spokas KA (2010) Review of the stability of biochar in soils: predictability of O: C molar ratios, Carbon Manag 1:289–303. https://doi.org/10.4155/cmt.10.32
- 38. Howell A, Helmkamp S, Belmont E (2022) Stable polycyclic aromatic carbon (SPAC) formation in wildfire chars and engineered biochars. Sci Total Environ 849:157610. https://doi.org/10.1016/j.scitotenv.2022.157610
- 39. Branca C, Di BC (2013) A unified mechanism of the combustion reactions of lignocellulosic fuels. Thermochim Acta 565:58–64. https://doi.org/10.1016/j.tca.2013.04.014
- Miller RS, Bellan J (1997) A generalized biomass pyrolysis model based on superimposed cellulose, hemicellulose and lignin kinetics. Combust Sci Technol 126:97–137. https://doi.org/10.1080/00102209708935670
- 41. Di Blasi C, Buonanno F, Branca C (1999) Reactivities of some biomass chars in air. Carbon N Y 37:1227–1238. https://doi.org/10.1016/S0008-6223(98)00319-4
- 42. Amini E, Safdari MS, Johnson N, Weise DR, Fletcher TH (2021) Pyrolysis kinetics of wildland vegetation using model-fitting methods. J Anal Appl Pyrolysis . https://doi.org/10.1016/j.jaap.2021.105167
- 43. De Caprariis B, Laura M, Marco S, Herce C, Verdone N, De Filippis P (2015) Kinetic analysis of biomass pyrolysis using a double distributed activation energy model. J Therm Anal Calorim . https://doi.org/10.1007/s10973-015-4665-2
- 44. Tihay V, Santoni P, Simeoni A, Garo J, Vantelon J (2009) Skeletal and global mechanisms for the combustion of gases released by crushed forest fuels Skeletal and global mechanisms for the combustion of gases released by crushed forest fuels. Combust Flame 156:1565–1575. https://doi.org/10.1016/j.combustflame.2009.05.004
- 45. Tihay V, Simeoni A, Garo JP, Laboratory-II (2009) Determination of a global combustion mechanism for flaming in forest fire modelling
- 46. Tihay V, Gillard P (2011) Comparison of several kinetic approaches to evaluate the pyrolysis of three Mediterranean forest fuels. Int J Therm Sci 20:407–417
- 47. Yoon HC, Pozivil P, Steinfeld A (2012) Thermogravimetric pyrolysis and gasification of lignocellulosic biomass and kinetic summative law for parallel reactions with. Energy Fuels 26:357–364. https://doi.org/10.1021/ef201281n
- 48. Sonobe T, Worasuwannarak N (2008) Kinetic analyses of biomass pyrolysis using the distributed activation energy model. Fuel 87:414–421. https://doi.org/10.1016/j.fuel.2007.05.004

- 49. Arenas CN, Navarro MV, Martinez JD (2019) Pyrolysis kinetics of biomass wastes using isoconversional methods and the distributed activation energy model. Bioresour Technol . https://doi.org/10.1016/j.biortech.2019.121485
- 50. Zhang J, Chen T, Wu J, Wu J (2014) Multi-Gaussian-DAEM-reaction model for thermal decompositions of cellulose, hemicellulose and lignin: comparison of N_2 and CO_2 atmosphere. Bioresour Technol 166:87–95. https://doi.org/10.1016/j.biortech.2014.05.030
- 51. Serbănescu C (2014) Kinetic analysis of cellulose pyrolysis: a short review. Chem Pap 68:847–860. https://doi.org/10.2478/s11696-013-0529-z
- 52. Ranzi E, Corbetta M, Manenti F, Pierucci S (2014) Kinetic modeling of the thermal degradation and combustion of biomass. Chem Eng Sci 110:2–12. https://doi.org/10.1016/j.ces.2013.08.014
- 53. Kawamoto H (2016) Review of reactions and molecular mechanisms in cellulose pyrolysis. Curr Org Chem 20:1–1. https://doi.org/10.2174/2213337203666160525102910
- 54. Tihay V, Santoni P-A, Simeoni A, Garo J-P, Vantelon J-P (2009) Skeletal and global mechanisms for the combustion of gases released by crushed forest fuels. Combust Flame 156:1565–1575. https://doi.org/10.1016/j.combustflame.2009.05.004
- 55. Benkoussas B, Consalvi JL, Porterie B, Sardoy N, Loraud JC (2007) Modelling thermal degradation of woody fuel particles. Int J Therm Sci 46:319–327. https://doi.org/10.1016/j.ijthermalsci.2006.06.016
- 56. Chen D, Zheng Y, Zhu X (2013) In-depth investigation on the pyrolysis kinetics of raw biomass. Part I: kinetic analysis for the drying and devolatilization stages. Bioresour Technol 131:40–46. https://doi.org/10.1016/j.biortech.2012.12.136
- 57. Poletto M, Zattera AJ, Santana RMC (2012) Thermal decomposition of wood: kinetics and degradation mechanisms. Bioresour Technol 126:7–12. https://doi.org/10.1016/j.biortech.2012.08.133
- 58. Shen DK, Gu S, Jin B, Fang MX (2011) Thermal degradation mechanisms of wood under inert and oxidative environments using DAEM methods. Bioresour Technol 102:2047–2052. https://doi.org/10.1016/j.biortech.2010.09.081
- 59. Korobeinichev OP, Paletsky AA, Gonchikzhapov MB, Shundrina IK, Chen H, Liu N (2013) Combustion chemistry and decomposition kinetics of forest fuels. Procedia Eng 62:182–193. https://doi.org/10.1016/j.proeng.2013.08.054
- 60. Gollner MJ, Miller CH, Tang W, Singh AV (2017) The effect of flow and geometry on concurrent flame spread. Fire Saf J 91:68–78. https://doi.org/10.1016/j.fire-saf.2017.05.007
- 61. Nelson RM (2003) Reaction times and burning rates for wind tunnel headfires. Int J Wildl Fire 12:195–211. https://doi.org/10.1071/WF02041
- 62. Rousset P, MacEdo L, Commandré JM, Moreira A (2012) Biomass torrefaction under different oxygen concentrations and its effect on the composition of the solid by-product. J Anal Appl Pyrolysis 96:86–91. https://doi.org/10.1016/j.jaap.2012.03.009
- 63. Wang H, Van Eyk PJ, Medwell PR, Birzer CH, Tian ZF, Possell M (2017) Effects of oxygen concentration on radiation-aided and self-sustained smoldering combustion of radiata pine. Energy Fuels 31:8619–8630. https://doi.org/10.1021/acs.energyfuels.7b00646
- 64. Thomas JC, Hadden RM, Simeoni A (2017) Experimental investigation of the impact of oxygen flux on the burning dynamics of forest fuel beds. Fire Saf J 91:855–863. https://doi.org/10.1016/j.firesaf.2017.03.086
- 65. Watson, Andrew J., Lovelock JE (2013) The dependence of flame spread and probability of ignition on atmospheric oxygen. In: Fire Phenomena and the earth system: an interdisciplinary guide to fire science. Wiley, New York

- 66. Joshi AK, Kumar A, Raghavan V, Trubachev SA, Shmakov AG, Korobeinichev OP, Kumar BP (2021) Numerical and experimental study of downward flame spread along multiple parallel fuel sheets. Fire Saf J 125:103414. https://doi.org/10.1016/j.fire-saf.2021.103414
- 67. Shotorban B, Yashwanth BL, Mahalingam S, Haring DJ (2018) An investigation of pyrolysis and ignition of moist leaf-like fuel subject to convective heating. Combust Flame 190:25–35. https://doi.org/10.1016/j.combustflame.2017.11.008
- 68. Pickett BM, Isackson C, Wunder R, Fletcher TH, Butler BW, Weise DR (2010) Experimental measurements during combustion of moist individual foliage samples. Int J Wildl Fire 19:153–162. https://doi.org/10.1071/WF07121
- 69. Surawski NC, Sullivan AL, Meyer CP, Roxburgh SH, Polglase PJ (2015) Greenhouse gas emissions from laboratory-scale fires in wildland fuels depend on fire spread mode and phase of combustion. Atmos Chem Phys 15:5259–5273. https://doi.org/10.5194/acp-15-5259-2015
- 70. Doerr SH, Santín C, Merino A, Belcher CM, Baxter G (2018) Fire as a removal mechanism of pyrogenic carbon from the environment: effects of fire and pyrogenic carbon characteristics. Front Earth Sci 6:1–13. https://doi.org/10.3389/feart.2018.00127
- 71. Finney MA, Forthofer J, Grenfell IC, Adam BA, Akafuah NK, Saito K (2015) Fire and explosion—a study of flame spread in engineered cardboard fuel beds part I: correlations and observations of flame spread. Prog Scale Model Vol II Sel from Int Symp Scale Model ISSM VI ISSM VII . https://doi.org/10.1007/978-3-319-10308-2 5
- 72. He Q, Liu N, Xie X, Zhang L, Zhang Y, Yan W (2021) Experimental study on fire spread over discrete fuel bed—Part I: effects of packing ratio. Fire Saf J 126:103470. https://doi.org/10.1016/j.firesaf.2021.103470
- 73. Fang JB, Steward FR (1969) Flame spread through randomly packed fuel particles. Combust Flame 13:392–398. https://doi.org/10.1016/0010-2180(69)90108-4
- 74. Turns SR (2012) Chapter 3: introduction to mass transfer. An introduction to combustion: concepts and applications, 3rd edn. McGraw-Hill Companies Inc, New York, pp 79–101
- 75. Bergman TL, Lavine AS, Incropera FP, Dewitt DP (2011) Chapter 14: diffusion mass transfer. Fundamentals of heat and mass transfer, 3th edn. Wiley, New York, pp 934–971
- 76. Turns SR (2012) Chapter 7: simplified conservation equations for reacting flows. An introduction to combustion: concepts and applications, 3rd edn. McGraw-Hill Compnaies Inc, New York, pp 221–252
- 77. Catchpole EA, Catchpole WR, Rothermel RC (1993) Fire behavior experiments in mixed fuel complexes. Int J Wildl Fire 3:45–57. https://doi.org/10.1071/WF9930045
- 78. Meroney RN, Bradshaw P (1975) Turbulent boundary-layer growth over a longitudinally curved surface. AIAA J 13:1448–1453
- 79. Clark TL, Reeder MJ, Griffiths M, Packham D, Krusel N (2005) Infrared observations and numerical modelling of grassland fires in the Northern Territory, Australia. Meteorol Atmos Phys 88:193–201. https://doi.org/10.1007/s00703-004-0076-9
- 80. Clark TL, Radke L, Coen J, Middleton D (1999) Analysis of small-scale convective dynamics in a crown fire using infrared video camera imagery. J Appl Meteorol 38:1401–1420. https://doi.org/10.1175/1520-0450(1999)038<1401:AOSSCD>2.0.CO;2
- 81. Sarie WS (1994) Further © 1994. 379-409
- 82. Maughan JR, Incropera FP (1987) Secondary flow in horizontal channels heated from below. Exp Fluids 5:334–343. https://doi.org/10.1007/BF00277712
- 83. Block JA (1971) A theoretical and experimental study of nonpropagating free-burning fires. Symp Combust 13:971–978. https://doi.org/10.1016/S0082-0784(71)80097-8

Publisher's Note Springer Nature remains neutral with regard to jurisdictional claims in published maps and institutional affiliations.

Springer Nature or its licensor (e.g. a society or other partner) holds exclusive rights to this article under a publishing agreement with the author(s) or other rightsholder(s); author self-archiving of the accepted manuscript version of this article is solely governed by the terms of such publishing agreement and applicable law.